

# Relativistic High-order Harmonic Beam Directionality Modulation by Pre-plasma Density Distribution

CHAONENG WU<sup>1,2</sup>, YIMING XU<sup>2,3</sup>, JAISMEEN KAUR<sup>4</sup>, ANDRE KALOUGUINE<sup>4</sup>, ANTOINE CAVAGNA<sup>4</sup>, STEFAN HAESSLER<sup>4</sup>, ZUOYE LIU<sup>3</sup>, RODRIGO LOPEZ-MARTENS<sup>4</sup>, CANGTAO ZHOU<sup>1,2,\*</sup>, PHILIPPE ZEITOUN<sup>4</sup>, LU LI<sup>2,\*</sup>

<sup>1</sup> College of Physics and Optoelectronic Engineering, Shenzhen University, Shenzhen 518060, China

<sup>2</sup> Shenzhen Key Laboratory of Ultraintense Laser and Advanced Material Technology, Center for Intense Laser Application Technology, and College of Engineering Physics, Shenzhen Technology University, Shenzhen 518118, China

<sup>3</sup> Frontiers Science Center for Rare Isotopes and School of Nuclear Science and Technology, Lanzhou University, 730000 Lanzhou, China

<sup>4</sup> Laboratoire d'Optique Appliquée, ENSTA ParisTech—École Polytechnique IP Paris- CNRS UMR—7639, Palaiseau, France

\*[zhoucangtao@sztu.edu.cn](mailto:zhoucangtao@sztu.edu.cn)

\*[lilu@sztu.edu.cn](mailto:lilu@sztu.edu.cn)

Received XX Month XXXX; revised XX Month, XXXX; accepted XX Month XXXX; posted XX Month XXXX (Doc. ID XXXXX); published XX Month XXXX

The use of a tunable pre-pulse is a common technique to enhance the high-order harmonic generation from surface plasma. The dynamic and structure of a pre-plasma is influenced by the intensity of ionization, heating, and expansion. Time delay between the pre-pulse and the main pulse serves as a crucial parameter for controlling the distribution of the pre-plasma density. The variation in harmonic emission directionality due to the density shape is investigated. Particle-in-cell simulations suggest that both plasma hydrodynamics and geometrical optical effect induces the deflection of harmonic beam from specular reflection. This research contributes to advancing the understanding of laser-plasma interaction conditions, which is important for the detection and optimizing of harmonic source performance.

The advancement of laser technology has facilitated the generation of relativistic electro-magnetic fields capable of generating extreme ultraviolet (XUV) radiation via laser-driven plasma surfaces. The surface high-order harmonic generation (SHHG) has the advantage on avoiding the driving field intensity threshold [1] and high conversion efficiency [2, 3], allowing to deliver ultra-intense attosecond pulses at XUV to X-ray region. Extensive researches have been dedicated to elucidating the mechanisms of SHHG [3, 4], including coherent wake emission (CWE), relativistic oscillating mirror (ROM), and coherent synchrotron emission (CSE). In the past fifteen years, the SHHG source development has evolved from physical understanding to characterization and field manipulation. Spectral, spatial, temporal characterizations and modulation via laser-plasma interaction control are crucial for the source application. Notably, ptychography [5] and the Spectral Phase Interferometry for Direct Electric-Field Reconstruction (SPIDER) [6] method have been proposed to accurately characterize the spatial and spectral phase for the SHHG source. Concerning harmonic source modulation, optimization of conversion efficiency is closely related with the temporal modulation techniques. These include two-color field enhancement of harmonic spectra [8]

and optimization using tailored multi-color driving lasers [9]. For simple Gaussian driving beams, the plasma density distribution plays an important role in controlling harmonic qualities [10]. The SHHG process is particularly sensitive to density gradient at the plasma-vacuum boundary [11]. Moreover, the spatial properties of SHHG sources at relativistic region are influenced by the plasma denting effect, which significantly alters the critical surface [12, 13]. Methods proposed to compensate for spatial degradations include plasma truncation with an extra pre-pulse [14], slightly moving the target out of focus for near-field wave front compensation [15] and using a convex target to achieve a flat surface despite plasma denting-induced concavity [16].

Experimental approaches to create a controllable steep pre-plasma profile have been widely developed. Typically, a small fraction of the laser energy is diverted from the main beam using a holey or pick-up mirror along the transmission line prior to reaching the focal spot [17]. The small pre-pulse beam and the larger main beam then follow the same optical path, ensuring the main beam to be accurately positioned at the plasma-vacuum boundary. Essentially, the harmonic signal is collected in the specular reflection direction, hundreds of millimeters distant from the laser-plasma interaction point, within the far-field region of the harmonic beam. The harmonic signal typically exhibits a divergence

angle ranging from tens to 100mrad [12]. For flatfield spectrometer [18] or applications involving reflection of the XUV pulse off a mirror at a grazing incidence angle, precise control of beam directionality is pivotal.

The harmonic characteristics, including directionality, have been the subject of theoretical and experimental studies over the past few decades. However, a common limitation of current theories is the assumption of an 1D plasma density distribution, which is typically modeled as a transversely uniform exponential decay profile. Practically, the pre-pulse induced plasma density gradient can exhibit significant lateral spatial variations, leading to an initial reflecting surface with a tilt. When the main pulse interacts with this tilted surface, the harmonic beam deviates from the specular direction.

To demonstrate this effect, a Gaussian pre-plasma density profile is considered. Any misalignment of the pre-pulse can result in a substantial displacement of the main pulse on the pre-plasma. Even under ideal optical conditions, the thermal expansion of the pre-plasma contributes to the angular deviation, as depicted in Fig. 1(a). The target is placed on x-z plane, while y axis is perpendicular to the target. Considering the laser ray lies on x-y plane for simplicity, the problem can be solved on the x-y 2D plane. Note that we can simply extend the following theory to obtain comprehensive 3D results. The pre-pulse and main pulse are illustrated by the lighter and darker red cones, respectively. The plasma region, where the density exceeds the critical density ( $n_e = n_c \cos^2 \theta$ ), is highlighted in purple. The plasma expansion velocity is known to increase with the pre-pulse fluence [17,19] In this study, the Gaussian approximation is given by

$$n_e(x, y) = n_0 \left( \exp \left( -\frac{y}{L(x)} \right) - 1 \right),$$

$$L(x) = L_0 \exp -\frac{x^2}{w_{pre}^2}, \quad (1)$$

where  $L = \left[ \frac{1}{n_e} \left( \frac{dn_e}{dy} \right) \right]^{-1}$ .  $n_e$  is the electron density profile,  $x$  is the distance along solid surface to the beam center, and  $y$  is the distance from the initial solid surface before thermal expansion,  $w_{pre}$  is the 1/e-radius of the pre-plasma gradient scale length profile.

To elucidate the impact of the Gaussian pre-pulse on the reflected beam, we initially regard the critical surface as a static and perfect reflector. Upon the main pulse striking the pre-plasma at an oblique angle ( $L \neq 0$ ), the interaction point between the laser and plasma occurs where the Gaussian-shaped critical surface intersects with the central axis of the main pulse's optical path. Using the scenario without a pre-plasma ( $L_0 = 0$ ) as a benchmark to measure beam deviation caused by geometric tilt, the XUV beam propagates along the specular reflection, indicated by the purple dashed lines. To address the beam deviation when a pre-plasma is presented ( $L_0 \neq 0$ ), the location of the reflection is determined by calculating the intersection between the geometric critical surface  $y_1(x)$  and the light ray path equation (Eq.)  $y_2(x)$ , which are represented as:

$$y_1(x) = L_0 \exp -\frac{x^2}{w_{pre}^2} \ln \left( \frac{n_0/e}{n_c \cos^2 \theta} \right), y_2(x) = \frac{x - x_0}{\tan \theta} \quad (2)$$

In this context,  $n_0$  represents the peak density at the solid target,  $y_1$  is obtained with the assumption that the surface with  $n_e = n_0/e$  stays at original solid-vacuum boundary for the laser heating area [P. Mora, *Plasma Expansion into a Vacuum*, PRL **90**, 185002 (2003)].  $\theta$

signifies the angle of incidence, and  $x_0$  is the lateral distance of the focal point of the main pulse to the center of the Gaussian pre-plasma distribution, shown in Fig. 1(a). Eq. (2) can be simplified with the assumption that  $x_0 L_0 / w_{pre}^2 \ll 1$ , which always hold true when dealing with a typical SHHG process. The simplified solution is thus  $x_r = x_0 + y_1(x_0) \tan \theta$ , where  $x_r$  is the transverse coordinate of the intersection spot. The solution can be verified theoretically by compared to the strict solution at  $x_0 = 0$ , written as  $x_r = \frac{w_{pre} \sqrt{W(g^2)}}{\sqrt{2}}$ ,  $y_r = \frac{x_r}{\tan \theta}$ , where  $g = \frac{\sqrt{2} L_0 \tan \theta}{w_{pre}} \ln \left( \frac{n_0/e}{n_c \cos^2 \theta} \right)$ , and  $W(x)$  is the Lambert W function.

The deviation angle  $\alpha$ , which quantifies the deviation from the expected reflection point due to the pre-plasma influence on the main pulse interaction with the target, depicted in Fig. 1(a), was used to characterize the geometrical tilt. The angle equation caused by the Gaussian pre-plasma can be expressed as

$$\alpha = 2 \arctan \frac{dy(x)}{dx} \Big|_{x=x_r} \approx 2 \ln \frac{n_0/e}{n_c \cos^2 \theta} \delta(x_r) \quad (3)$$

where the slope  $\delta(x_r)$  is defined as  $\delta(x) = dL/dx$ . It is a more universal indicator for the pre-plasma tilt than the specific  $L$  and  $w_{pre}$  in the optical model, written as:

$$\delta = -\frac{2x_r}{w_{pre}^2} L(x_r) \quad (4)$$

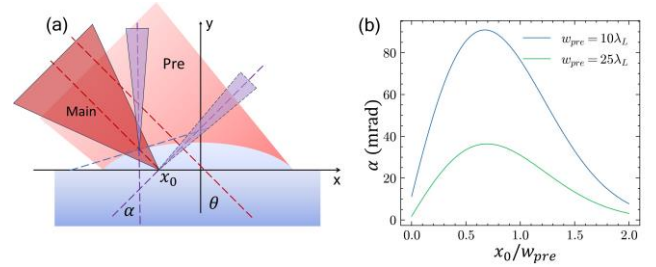


Fig. 1. (a) Schematic for the origin of pre-plasma tilt: the interaction between a Gaussian distributed pre-plasma and the main pulse. The light red beam represents the pre-pulse, and the dark red beam indicates the main pulse. For clarity in the figure, the main pulse has been exaggerated in size. The purple lines signify the reflection directions with and without pre-plasma. (b) angle deviation induced by the geometrical tilt at different focal positions.

According to the focal position of main pulse  $x_0$  and the density distribution,  $L$  and  $\delta$  can be regarded as two independent indicators for describing the pre-plasma condition in the main pulse focus. The geometrical deviation angle  $\alpha$  can be calculated according to Eq. 3. Fig. 1(b) shows the deviation angle  $\alpha$  at different incident position for two different pre-plasma conditions: a narrow pre-plasma profile as  $w_{pre} = 10\lambda_L$  and a normal one as  $w_{pre} = 25\lambda_L$ ,  $\theta = \pi/4$  and  $L = 0.1\lambda_L$  are the same in these two cases. Assuming a  $n_0/e = 100n_c$  surface was generated by the pre-pulse, which is close to the case of a fully ionized  $\text{SiO}_2$ . The geometrical deviation angle comes to tens of milliradians at  $x_r = w_{pre}/\sqrt{2}$ , which can be obviously observed in experiment. It might move the far-field beam spot out of the collecting system such as flatfield spectrometer. While the deviation angle at  $x_0 = 0$  is relatively small even with the rather narrow pre-plasma profile, the  $\delta$  at the

flank of pre-plasma will be considered as the main reason for the origin of surface tilt, which gives a maximum value of  $\sim 0.008$  for the narrow pre-plasma profile

The above optical model causes the geometrical angle deviation. However, upon the incidence of a relativistic, tightly focused short pulse, the reflection does not happen at a fixed surface but is caused by a dynamic compressed electron sheet driven around the solid density region. This compression modifies the reflection spot relative to the original surface position, introducing a correction to the geometrical tilt. To assess the impact of the plasma effect on the directionality of the harmonic source, particle-in-cell (PIC) simulations were conducted, aiming to explore the collective effects and influence on the tilt angle. Simulations shows that actual tilt angle observed on the reflected pulse is reduced compared to the geometrical tilt angle, suggesting a correction coefficient that is less than 1 should be applied to the right side of Eq. (3). The modulation of harmonics directionality serves as a universal indicator for the pre-plasma critical surface tilt. The dynamics of the tilt can be inferred from the angular deviation of the beam drift, which in turn can be employed to characterize the plasma expansion process within a pump-probe like scheme, where the pump is the pre-pulse and the probe is SHHG pulse. This approach provides valuable insights into the behavior of the plasma under the influence of the driving laser field and its subsequent effect on the spatial coherence of the emitted harmonics.

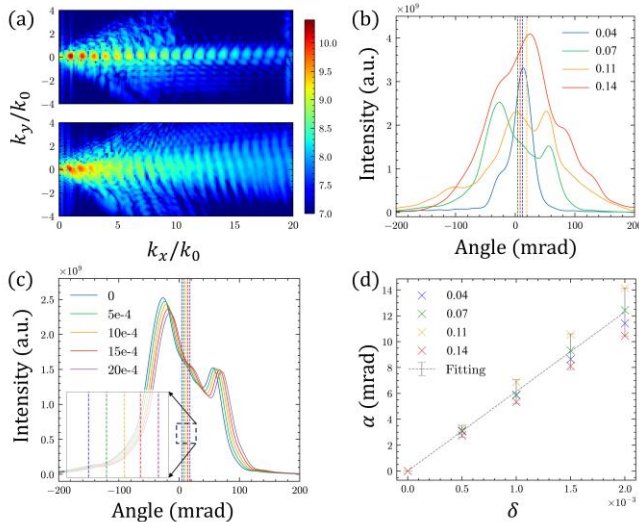


Fig. 2 Simulation results for different scale length  $L$  and decay slope  $\delta$ . (a) 2D spectrum of  $L = 0.04$  and  $0.14$ , (b) lineouts of far-field angular spectrum map driven by different scale lengths, the centroid of harmonic spectrum is shown in dashed lines, (c) the spectrum drift caused by increasing  $\delta$ , the centroid of spectrum is shown in dashed lines and zoomed in in the inset figure. (d) the simulated angular drift by different decay slope, the fitting linear relationship is shown with error bar, which indicates for  $d\alpha/d\delta = 6.1 \pm 0.9$ .

PIC simulations have been carried out with WarpX code, as sketched in Fig. 2(a). A p-polarized laser is injected from the left boundary into the simulation box, with a beam waist of  $w_0 = 1.5\lambda_L$  and a duration of  $\tau = 2T_0$ . Here,  $\lambda_L = 800$  nm and  $T_0 = \lambda_L/c$  represent the fundamental laser wavelength and period, respectively. The normalized vector potential is  $a_0 = 2.5$  and the

incidence angle is chosen as  $\theta = 45^\circ$ . The target consists of a fully ionized carbon slab with a thickness of  $2\lambda_L$ . The pre-plasma follows the Gaussian profile in Eq. 1, and a maximum density of  $n_{max} = 100e \times n_c$  and  $L = 0.07\lambda_L$  was used to simulate a solid density target. Note that the density details higher than  $n_e = n_0/e$  was ignored and represented by a uniform density of  $n_0/e$ , while in our case the plasma denting depth is smaller than the distance from critical surface to the  $n_0/e$  surface. And the  $\cos \theta$  was used to simplify simulation parameter. The simulation grid size is set to  $\lambda_L/512$ , and 100 particles per cell are used for resolving up to the 30<sup>th</sup> order harmonic signals. With a slope  $\delta$ , the scale length  $L(x)$  of pre-plasma varies with  $x$  as according to  $L = L_c + \delta x$ , where  $L_c$  is the central scale length at  $x = 0$ . Typical results with  $L_c/\lambda_L = 0.04, 0.07, 0.11, 0.14$  and  $10^4\delta = 5, 10, 15, 20$  are shown in Fig. 2. The beam drift was quantified through the angular distribution of the simulated harmonics. A near-field-to-far-field transformation was applied to project the reflected harmonic beam from the simulation domain into the far-field. Subsequently, the drift angle  $\alpha$  was determined by the displacement from the specular reflection direction of the centroid of the high-order harmonic ( $n > 10$ ). The simulated near-field spectrum for  $L_c = 0.07, \delta = 0$  and  $L_c = 0.14, \delta = 0$  are displayed in Fig. 2(a) as an example. The corresponding far-field angular distributions for various  $L_c$  values with  $\delta = 0$ , were calculated by integrating the spectral intensity along each far-field angular direction and are shown in Figure 2(b). The centroid in the far-field angular distribution is shown by dashed line, which indicates the angular drift induced by the scale length variation. The inherent angle  $\alpha_0$  for the uniform target with  $\delta = 0$  was found to be 12 mrad, 4 mrad, 19 mrad and 8 mrad for the scale lengths  $L_c/\lambda_L = 0.04, 0.07, 0.11, 0.14$ , respectively. In this scenario, few-mrad level angular drifts from specular direction are observed caused by the morphing beam shape, which is independent to  $\delta$ . And it is relatively small compared to the overall angular divergence. Note that a very tightly focused driving beam is adopted in this work, and when it comes to the typical experimental results with an angular divergence of  $\sim 50$  mrad, the beam drift due to variations in  $L_c$  can be expected to be less than 5 mrad.

While the scale length  $L_c$  has a minimal impact on the beam directionality, the decay rate  $\delta$  influences the angular drift. With  $L_c$  set to  $0.07\lambda_L$ , the angular intensity distributions for various  $\delta$  values are depicted in Figure 2(c). The angular profile shifts uniformly across the four different slopes, demonstrating a linear relationship between the angular drift  $\alpha$  (with respect to  $\delta = 0$ ) and the slope  $\delta$ , in consistent with the prediction from Eq. (3). However, Figure 2(d) reveals that the linear slope factor  $k = d\alpha/d\delta$  remains constant across different scale lengths, yet it does not align with the value derived from Eq. (3) which predicts a linear factor of  $k_1 = 10.59$ , whereas the simulations suggest a factor close to  $6.1 \pm 0.9$ . This discrepancy suggests that there is an additional correction factor arising from the plasma effect that affects the geometrical angular deviation.

To elucidate the plasma correction, an analysis of the electron dynamics in the pre-plasma was conducted. The SHHG process can be divided into three distinct phases based on the motion of the reflecting surface: compression phase, acceleration phase, and dephasing phase. According to the plasma denting theory, electrons in the pre-plasma reach an equilibrium position at the end of the compression phase. It can be considered as an indicator for the emission spot. In the case of short pulse driving, the effect of the positive ion background motion can be neglected. The equilibrium



depth that the reflecting surface ultimately reaches, relative to the geometrical surface position [12], is given with a density truncation at  $n_c / \cos^2 \theta$  as:

$$y_e = -L \ln \left[ 1 + \frac{\lambda_L a_0 (1 + \sin \theta)}{\pi L} \frac{1}{\cos^2 \theta} \right], \quad (5)$$

The conclusion has been verified to be valid for our conditions without the truncation by only introducing a constant fix of  $0.01\lambda_L$  to  $y_e$ . Noted that  $y_1(x)$  in Eq. 1 is not limited to a Gaussian distribution, every function has its own geometrical decay slope, and thus the geometrical linear factor can be calculated from Equation (3). The plasma denting effect can thus provide a correction to the reflection position via  $dy_e(x)/dx$ . Since  $y_e$  is approximately linearly related to  $L$  while the main beam is small compare to the pre-plasma, it results in a nearly constant correction to the angle deviation  $\alpha \propto dy/dx$ .

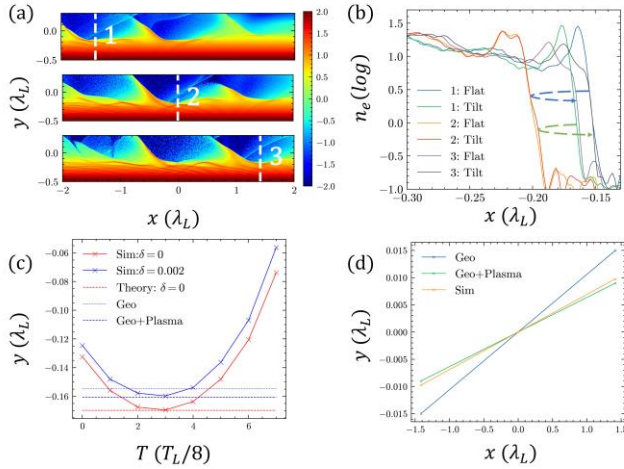


Fig. 3. Correction of decay slope on the geometrical profile by the plasma effect. (a) density maps driven by laser at different moment and (b) the corresponding lineouts at the equilibrium positions for  $\delta = 0$  and  $0.002$ , the dashed lines shows the equilibrium surface dynamics along  $x$  when laser swipes along target, blue represents for the flat target and green represents for the tilt one, (c) the reflecting surface motion around the end of compression phase for position 1, (d) denting depth difference between  $\delta = 0$  and  $0.002$ .

In physical terms, plasma denting flattens the slope  $\delta(x_r)$  because a larger scale length facilitates the pushing of the reflecting electron sheet further into the dense plasma region. When the laser swipes over the plasma surface in Fig. 3(a), the equilibrium depth difference between the tilt case with  $\delta \neq 0$  and the ideal uniform condition with  $\delta = 0$  can be regarded as the reason for the beam drift. Each panel shows a different moment for  $\delta = 0.002$ , the temporal interval is the cycle of incident laser, while the center panel gives the density map when the equilibrium spike reaches  $x = 0$ . The equilibrium position for the three positions in Fig. 3(a) is plotted in Fig. 3(b). To exhibit how  $\delta$  works to produce a reflection surface tilt, the equilibrium density profiles with  $\delta = 0$  at the same moments and positions are also plotted as a reference. It can be observed that there is no difference at the beam center, and surface in flat case start from a shallow position and end at a deeper position, which is different with that of a tilt case. The reflecting

surface dynamics around the equilibrium position are depicted in Fig. 3(c). Using the equilibrium depth at  $x = 0$  (position-1 in Fig. 3(a)) as a reference, if the equilibrium depth at position-1 was calculated by only considering the geometrical tilt of the critical surface, the equilibrium depth should locate at the blue dotted line. Only if the correction by the plasma effect from  $dy_e(x)/dx$  was considered, the equilibrium depth can be predicted perfectly. That means that our combined theory with the geometrical tilt and plasma effect can be used to calculate the equilibrium depth for different spatial position. The relative difference between the equilibrium position of flat and tilt surface can be used to evaluate the correctness of Eq. 5, shown in Fig. 3(d). The combined theory predicts a tile equilibrium depth with spatial coordinate compared to the flattened one, and the slope is smaller than that with only the geometrical effect. The slope was evaluated by considering the depth difference at position-2 and position-3. Good agreement is shown between the theoretical and simulation results. Numerically speaking, the angle drift induced by the plasma denting correction can be expressed here for our simulation parameters as:

$$k_e = \frac{d}{d\delta} \left( 2 \arctan \frac{dy_e}{dx} \right) \approx 4.8, \quad (6)$$

Note that  $k_e$  varies with  $a_0$ , and here the result at  $x = \sqrt{2}\lambda_L$  was used as an averaged value. The combined angular drift is thus  $\alpha = (k_1 - k_e)\delta = 5.8\delta$ , which fits well the simulation results. Note that when a long driving pulse is used, a further correction should be considered to account for ion motion. The detailed correction from scale length and ion motion is out of scope of this article, and it will be studied in our next work.

In conclusion, this study has thoroughly examined the effects of SHHG beam drifting for various pre-plasma distributions. For SHHG driven by few-cycle laser, the deviation of the harmonic emission angle from the specular direction is primarily governed by the slope of the critical surface. The theory and observed phenomena indicate that the drifting of the harmonic beam can serve as a probe for the critical surface condition at the main pulse focal spot. When a high-contrast laser system is utilized, the geometrical tilt dynamics of the pre-plasma can be continuously measured with varying pre-pulse delays. Furthermore, SHHG beam drifting as well as the far-field wave front information carries information on the relativistic plasma at micrometer and femtosecond to picosecond scales.

**Funding.** National Natural Science Foundation of China (Grant No. 12205203, 11875092), Laserlab-Europe (LOA0024038);

**Acknowledgments.** We gratefully acknowledge Dr. Taiwu Huang, Dr. Libao Ju, Dr. Ran Li and Dr. Ke Jiang for fruitful discussion.

**Disclosures.** The authors declare no conflicts of interest.

**Data availability.** Data underlying the results presented in this paper are not publicly available at this time but may be obtained from the authors upon reasonable request.

## References

1. C. Thaury *et al.*, Nature Phys **3**, 424–429 (2007).
2. T. Baeva, S. Gordienko, and A. Pukhov, Phys. Rev. E **74**, 046404 (2006).
3. C. Thaury and F. Quéré, J. Phys. B **43**, 213001 (2010).
4. U. Teubner, and P. Gibbon, Rev. Mod. Phys. **81**, 445–479 (2009).
5. A. Leblanc, S. Kahaly, and F. Quéré, Nature Phys **12**, 301–305 (2016).
6. C. Wu, L. Li *et al.*, Opt. Express **30**, 389 (2022).

7. L. Li *et al.*, Opt. Lett. **45**, 4248 (2020)
8. M. Yeung *et al.*, Nature Photon. **11**, 32–35 (2017); L. Chopineau *et al.*, Phys. Rev. Research **4**, L012030 (2022).
9. M.R. Edwards, and J. Mikhailova, Phys. Rev. Lett. **117**, 125001 (2016).
10. M. Behmke *et al.*, Phys. Rev. Lett. **106**, 185002 (2011).
11. S. Kahaly *et al.*, Phys. Rev. Lett. **110**, 175001 (2013).
12. H. Vincenti *et al.*, Nature Commun. **5**, 3403 (2014).
13. H. Vincenti, Phys. Rev. Lett. **123**, 105001 (2019).
14. B. Y. Li. *et al.*, Phys. Rev. Lett. **128**, 244801 (2022).
15. J. Gao *et al.*, Phys. Rev. E **101**, 033202 (2020).
16. Y. Zhang, C. Zhong, S. Zhu *et al.*, New J. Phys. **24**, 033038 (2022).
17. J. Kaur *et al.* Rev. Sci. Instrum. **94**, 113002 (2023).
18. T. Kita *et al.*, Appl. Opt. **22**, 512- 513 (1983).
19. S. Monchocé *et al.*, Phys. Rev. Lett. **112**, 145008 (2014).